

This copy is for your personal, non-commercial use only.

If you wish to distribute this article to others, you can order high-quality copies for your colleagues, clients, or customers by [clicking here](#).

Permission to republish or repurpose articles or portions of articles can be obtained by following the guidelines [here](#).

The following resources related to this article are available online at www.sciencemag.org (this information is current as of December 15, 2011):

Updated information and services, including high-resolution figures, can be found in the online version of this article at:

<http://www.sciencemag.org/content/327/5966/665.full.html>

Supporting Online Material can be found at:

<http://www.sciencemag.org/content/suppl/2010/02/04/327.5966.665.DC1.html>

A list of selected additional articles on the Science Web sites **related to this article** can be found at:

<http://www.sciencemag.org/content/327/5966/665.full.html#related>

This article **cites 28 articles**, 1 of which can be accessed free:

<http://www.sciencemag.org/content/327/5966/665.full.html#ref-list-1>

This article has been **cited by** 2 article(s) on the ISI Web of Science

This article has been **cited by** 1 articles hosted by HighWire Press; see:

<http://www.sciencemag.org/content/327/5966/665.full.html#related-urls>

This article appears in the following **subject collections**:

Physics

<http://www.sciencemag.org/cgi/collection/physics>

energy ~ 20 GeV), although our measurements could suggest a higher contribution from IC photon seeds. In particular, assuming a starlight energy density of 1.4 eV cm^{-3} and a mean temperature of ~ 2300 K (29), we obtain a good description of the AGILE data (Fig. 2).

The AGILE measurements would be incompatible with the scenario of nucleonic gamma-ray production in the Vela TeV nebula in the frame of a single primary electron population. These models predict very faint GeV emission ($< 10^{30} \text{ erg s}^{-1}$) even when including synchrotron and IC emission from primary and secondary electrons produced by the inelastic nuclear scattering (16). On the other hand, the proposed additional electron component scenario described above leaves room for uncorrelated GeV-TeV emission, although the comprehensive multiwavelength two-component leptonic model (providing strong IC emission on a relatively dense photon field) seems to disfavor dominant nucleonic gamma-ray production. In fact, it has been found that the thermal particle density at the head of the cocoon, where bright VHE gamma-ray emission was found, is lower than that required by hadronic models by a factor of 6 (14).

The radio-emitting region mentioned above appears to be larger ($\sim 2^\circ \times 3^\circ$) than the AGILE nebula, possibly indicating that IC cooling in the GeV domain is important. However, the actual physical size of the GeV nebula could be larger than what we are able to resolve with the available photon statistics, because of the strong galactic gamma-ray emission affecting MeV-GeV energy bands. Instead, the AGILE nebula is similar in shape to the HESS nebula, which may suggest that the core of HE and VHE emission is produced in the same projected region of Vela X, even if different electron populations are involved. Indeed, different spots of bright radio emission (28), possibly associated to electrons injected at different stages of pulsar evolution, are embedded within the poorly resolved HE and VHE emission regions.

High-energy PWN emissions are thought to be a common phenomenon associated with young and energetic pulsars (30) because the IC emission of these PWNe arises mostly from scattering on CMBR and starlight fields, with no special environmental requirements. On the other hand, PWN emissions are expected to be much weaker than pulsed emission from the associated neutron star, especially in the GeV domain where most of the pulsar's spin-down energy is funneled. Indeed, despite a PWN gamma ray yield of $L_\gamma^{\text{PWN}} \approx 10^{-3} \times \dot{E}_{\text{rot}}$, to be compared with the typical gamma-ray pulsed luminosity of $L_\gamma^{\text{pulsed}} \approx 10^{-2}$ to $0.1 \times \dot{E}_{\text{rot}}$, our AGILE observation shows that 10,000-year-old PWNe can match the sensitivities of current GeV instruments.

Because the gamma-ray luminosity of the PWN is only a small fraction of the beamed emission from the neutron star, the PWN component is difficult to identify in weaker gamma-

ray pulsars, although it could account for a substantial part of the observed off-pulse flux. However, if the beamed emission does not intersect the line of sight to the observer, the PWN component, unhindered by the stronger pulsed emission, could be detectable. Energetic pulsars (e.g., $\dot{E}_{\text{rot}} \approx 10^{37} \text{ erg s}^{-1}$) can power PWNe with gamma-ray luminosities matching the flux ($\sim 10^{-8}$ to 10^{-7} photons $\text{cm}^{-2} \text{ s}^{-1}$; $E > 100$ MeV) of a class of unidentified EGRET sources (22), as well as a subset of those detected by AGILE and Fermi (31, 32), when placed within few kiloparsecs. The roughly isotropic emission from such undisturbed PWNe would not yield pulsations, and, as a class, they could contribute to the population of galactic unidentified sources still awaiting multiwavelength association (13, 33).

References and Notes

- J. H. Taylor, R. N. Manchester, A. G. Lyne, *Astrophys. J. Suppl. Ser.* **88**, 529 (1993).
- R. Dodson, D. Legge, J. E. Reynolds, P. M. McCulloch, *Astrophys. J.* **596**, 1137 (2003).
- H. Rishbeth, *Aust. J. Phys.* **11**, 550 (1958).
- K. W. Weiler, N. Panagia, *Astron. Astrophys.* **90**, 269 (1980).
- K. S. Dwarakanath, *J. Astrophys. Astron.* **12**, 199 (1991).
- C. B. Markwardt, H. B. Oegelman, *Nature* **375**, 40 (1995).
- C. B. Markwardt, H. B. Oegelman, *Astrophys. J.* **480**, 13 (1997).
- D. A. Frail, M. F. Bietenholz, C. B. Markwardt, H. Oegelman, *Astrophys. J.* **475**, 224 (1997).
- D. J. Helfand, E. V. Gotthelf, J. P. Halpern, *Astrophys. J.* **556**, 380 (2001).
- F. Aharonian et al., *Astron. Astrophys.* **448**, L43 (2006).
- R. Enomoto et al., *Astrophys. J.* **638**, 397 (2006).
- J. M. Blondin, R. A. Chevalier, D. M. Frieron, *Astrophys. J.* **563**, 806 (2001).
- O. C. de Jager, *Astrophys. J.* **658**, 1177 (2007).
- S. LaMassa, P. O. Slane, O. C. de Jager, *Astrophys. J.* **689**, L121 (2008).
- O. C. de Jager, P. O. Slane, S. LaMassa, *Astrophys. J.* **689**, L125 (2008).
- D. Horns, F. Aharonian, A. Santangelo, A. I. D. Hoffmann, C. Masterson, *Astron. Astrophys.* **451**, L51 (2006).
- A. Pellizzoni et al., *Astrophys. J.* **691**, 1618 (2009).
- A. Abdo et al., *Astrophys. J.* **696**, 1084 (2009).
- M. Tavani et al., *Astron. Astrophys.* **502**, 995 (2009).
- G. Kanbach et al., *Astron. Astrophys.* **289**, 855 (1994).
- D. J. Thompson, in *Cosmic Gamma-Ray Sources*, K. S. Cheng, G. E. Romero, Eds. (Kluwer, Dordrecht, Netherlands, 2005), pp. 149–168.
- R. C. D. L. Hartman et al., *Astrophys. J. Suppl. Ser.* **123**, 79 (1999).
- B. Aschenbach, *Nature* **396**, 141 (1998).
- F. Aharonian et al., *Astron. Astrophys.* **437**, L7 (2005).
- O. C. de Jager, A. K. Harding, P. Sreekumar, M. Strickman, *Astron. Astrophys.* **120** (suppl.), 441 (1996).
- P. A. Caraveo, A. De Luca, R. P. Mignani, G. F. Bignami, *Astrophys. J.* **561**, 930 (2001).
- H. Alvarez, J. Aparici, J. May, P. Reich, *Astron. Astrophys.* **372**, 636 (2001).
- A. S. Hales et al., *Astrophys. J.* **613**, 977 (2004).
- The stellar radiation field peak is generally assumed at $E \approx 1$ eV, well fitting the gamma-ray galactic diffuse emission; see, e.g., www.iasf-milano.inaf.it/~giuliani/public/thesis/node10.html.
- F. Mattana et al., *Astrophys. J.* **694**, 12 (2009).
- C. Pittori et al., *Astron. Astrophys.* **506**, 1563 (2009).
- A. Abdo et al., *Astrophys. J. Suppl. Ser.* **183**, 46 (2009).
- A. Pellizzoni et al., *AIP Conference Proceedings*, vol. 745, F. A. Aharonian, H. J. Voelk, D. Horns, Eds. (2nd International Symposium on High Energy Gamma-Ray Astronomy, Heidelberg) (American Institute of Physics, New York, 2005), pp. 371–376.
- The AGILE mission is funded by the Italian Space Agency with scientific and programmatic participation by the Italian Institute of Astrophysics and the Italian Institute of Nuclear Physics.

Supporting Online Material

www.sciencemag.org/cgi/content/full/science.1183844/DC1

SOM Text
Figs. S1 and S2

References

26 October 2009; accepted 15 December 2009

Published online 31 December 2009;

10.1126/science.1183844

Include this information when citing this paper.

Visualizing Critical Correlations Near the Metal-Insulator Transition in $\text{Ga}_{1-x}\text{Mn}_x\text{As}$

Anthony Richardella,^{1,2*} Pedram Roushan,^{1*} Shawn Mack,³ Brian Zhou,¹ David A. Huse,¹ David D. Awschalom,³ Ali Yazdani^{1†}

Electronic states in disordered conductors on the verge of localization are predicted to exhibit critical spatial characteristics indicative of the proximity to a metal-insulator phase transition. We used scanning tunneling microscopy to visualize electronic states in $\text{Ga}_{1-x}\text{Mn}_x\text{As}$ samples close to this transition. Our measurements show that doping-induced disorder produces strong spatial variations in the local tunneling conductance across a wide range of energies. Near the Fermi energy, where spectroscopic signatures of electron-electron interaction are the most prominent, the electronic states exhibit a diverging spatial correlation length. Power-law decay of the spatial correlations is accompanied by log-normal distributions of the local density of states and multifractal spatial characteristics.

Since Anderson first proposed 50 years ago that disorder could localize electrons in solids (1), studies of the transition between extended and localized quantum states have been at the forefront of physics (2). Real-

izations of Anderson localization occur in a wide range of physical systems from seismic waves to ultracold atomic gases, in which localization has recently been achieved with random optical lattices (3). In electronic systems, the

signatures of localization have long been examined through electrical transport measurements (4, 5), and more recently by local scanning probe techniques that have imaged localized electronic states (6, 7). For noninteracting systems, the electronic states at the mobility edge are predicted to have a diverging localization length with scale-independent power-law characteristics, which are described as being multifractal (8). Given the poorly understood nature of the metal-insulator transition in the presence of disorder and electron-electron interactions, direct imaging of electronic states can provide insights into the interplay between localization and interactions.

We report on scanning tunneling microscopy (STM) and spectroscopy studies of electronic states in the dilute magnetic semiconductor $\text{Ga}_{1-x}\text{Mn}_x\text{As}$, over a range of Mn concentrations near the metal-insulator transition ($x = 1.5$ to 5%). Over the past decade, $\text{Ga}_{1-x}\text{Mn}_x\text{As}$ has emerged as a promising material for spintronic applications with a high ferromagnetic transition temperature (9, 10). Mn atoms substituted at Ga sites act both as acceptors that drive the metal-insulator transition and as localized spins that align at low temperatures to give rise to magnetism. The nature of the electronic states underlying magnetism in these heavily doped semiconductors is still debated. It is often assumed that the carriers that mediate magnetism in $\text{Ga}_{1-x}\text{Mn}_x\text{As}$ are Bloch states associated with either the valence bands or extended states originating from an impurity band (11–13); however, the validity of these assumptions has been questioned (14, 15). Moreover, many recent low-temperature transport studies show evidence of electron-electron interaction and weak localization of carriers even for samples with high doping levels (16–19). We used atomic-scale imaging and high-resolution spectroscopy with the STM to visualize electronic states in $\text{Ga}_{1-x}\text{Mn}_x\text{As}$ and to examine the spatial structure of electron-electron correlations in this system. Our results indicate that spatial heterogeneity and electronic correlations must be considered in understanding the mechanism of magnetism in highly doped semiconductors.

Figure 1 shows STM topographs of cleaved $\text{Ga}_{1-x}\text{Mn}_x\text{As}$ samples (2000 Å thick) grown by molecular beam epitaxy on a p-type Be-doped GaAs buffer layer (20, 21). Before measurements at a temperature of 4.2 K, the degenerately doped substrates are cleaved in situ to expose a (110) or equivalent surface of the heterostructure in cross section (Fig. 1A, inset). The topographs show in-gap states, dominated by individual Mn acceptor wave functions, although other defects such as As antisites are observed

as well. Using previous STM studies of samples with more dilute Mn concentrations (22, 23) and the results of tight-binding model calculations (21, 24, 25), we can identify the topographic signatures of individual Mn acceptors in layers from the surface to the third subsurface layer (Fig. 1B). The size of an individual Mn acceptor state wave function is about 20 Å, due to its deep binding energy, which results in a metal-insulator transition at a relatively high level of doping (between 1 and 2%) in $\text{Ga}_{1-x}\text{Mn}_x\text{As}$. By increasing the Mn concentration from weakly insulating samples with variable-range hopping resistivity at 1.5% (critical temperature $T_C = 30$ K) (19, 21) to relatively conducting samples at 5% ($T_C = 86$ K, annealed), we find that higher concentrations of dopants appear in STM topographs on top of the atomically ordered GaAs lattice (Fig. 1C). All characteristic lengths, such as dopant separation or mean free path (~ 10 Å), are much shorter for $\text{Ga}_{1-x}\text{Mn}_x\text{As}$ compared with other semiconductors doped with shallow dopants (15).

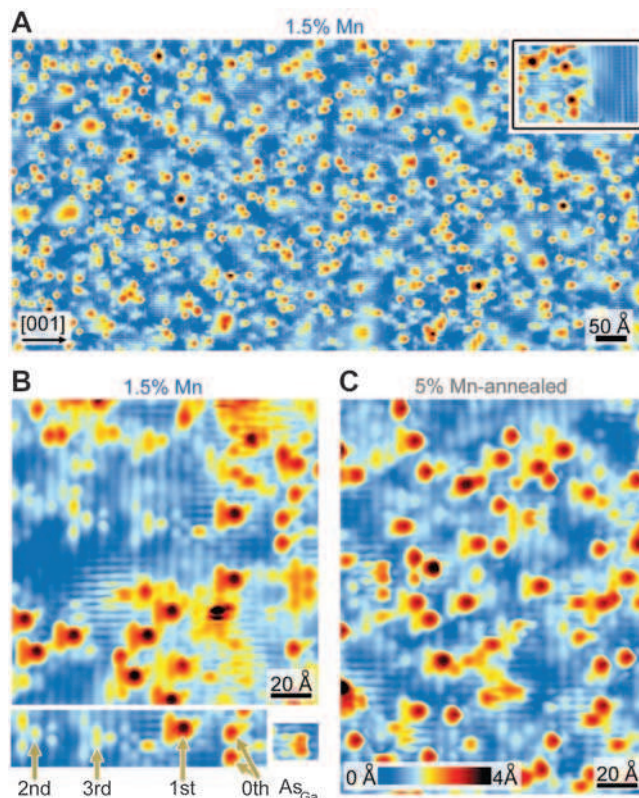
Spectroscopic mapping with the STM can be used to show that Mn acceptors and other defects give rise to atomic-scale fluctuations in the local electronic density of states (LDOS) over a wide range of energies. Figure 2A shows tunneling spectra of states from within the valence band (with the voltage $V < 0$) to the conduction band edge ($V > 1.5$), measured along a line perpendicular to the buffer layer-film interface. By contrasting the spatial dependence of electronic states in the buffer layer (with 2×10^{18} per cm^3 Be acceptors) to those of $\text{Ga}_{1-x}\text{Mn}_x\text{As}$ (with $x = 0.015$) in Fig. 2A, we find the Mn-doped region

to have strong spatial variations in the electronic states at the valence and conduction band edges and a broad distribution of states within the GaAs band gap. Increasing the Mn concentration gives rise to a larger number of in-gap states (compare Fig. 2, B and C). These features of the local electronic structure of $\text{Ga}_{1-x}\text{Mn}_x\text{As}$ are difficult to reconcile with a weakly disordered valence or impurity band picture and show the importance of compensation and disorder in this compound. The Fermi energy E_F lies within the range of electronic states that are spatially inhomogeneous.

In addition to strong spatial variations, electronic states of $\text{Ga}_{1-x}\text{Mn}_x\text{As}$ are influenced by electron-electron interactions (Fig. 2D). STM spectra, spatially averaged across large areas for several samples with increasing doping levels, illustrate a strong suppression of the tunneling density of states near E_F . The evolution from weakly insulating (1.5%) to relatively conducting samples (5%) is well correlated with the increase in the density of states at the Fermi level, yet a suppression centered at E_F is observed at all doping levels. This feature is indicative of an Altshuler-Aronov correlation gap that is expected to occur in the tunneling density of states of a disordered material on the metallic side of the phase transition (26), appearing as a square-root singularity in the conductance near E_F (Fig. 2D). Previous spectroscopic measurements of $\text{Ga}_{1-x}\text{Mn}_x\text{As}$ with macroscopic tunneling junctions have also reported similar correlation gaps (16).

To determine whether there are any specific length scales associated with the spatial variation of the LDOS in $\text{Ga}_{1-x}\text{Mn}_x\text{As}$, we examine

Fig. 1. STM topography of the in-gap states of GaMnAs. **(A)** STM topograph (+1.5 V, 20 pA) of $\text{Ga}_{0.985}\text{Mn}_{0.015}\text{As}$ over a 1000 Å by 500 Å area. The inset shows a topograph (+1.8 V, 20 pA) of the heterostructure junction between the Mn- and Be-doped layers of GaAs. The size of this area is 80 Å by 125 Å. **(B)** A topograph (+1.5 V, 30 pA) over a smaller area of size 150 Å by 150 Å of $\text{Ga}_{0.985}\text{Mn}_{0.015}\text{As}$. Several substitutional Mn's in various layers are identified in the lower part of the panel and marked by the layer in which they appear, with the surface labeled as zero. An As antisite is also shown. **(C)** STM topograph (+1.5 V, 20 pA) of the $\text{Ga}_{0.95}\text{Mn}_{0.05}\text{As}$ sample after annealing for 6 hours at 200°C. The size of the area is 150 Å by 195 Å. (B) and (C) have the same scale.



¹Joseph Henry Laboratories and Department of Physics, Princeton University, Princeton, NJ 08544, USA. ²Department of Physics, University of Illinois at Urbana-Champaign, Urbana, IL 61801, USA. ³Center for Spintronics and Quantum Computation, University of California, Santa Barbara, CA 93106, USA.

*These authors contributed equally to this work.

†To whom correspondence should be addressed. E-mail: yazdani@princeton.edu

energy-resolved STM conductance maps. In Fig. 3, we show examples of such maps at different energies relative to E_F for the 1.5% doped sample. These maps show that, in addition to modulations on the length scales of individual acceptors, there are spatial structures in the LDOS with longer length scales. To characterize these variations, for each conductance map, we compute the angle-averaged autocorrelation function between two points separated by r , $C(E, r) =$

$1/(2\pi) \int d\theta \int d^2r' [g(E, \mathbf{r}) - g_0(E)] \times [g(E, \mathbf{r}' + \mathbf{r}) - g_0(E)]$, in which $g(E, \mathbf{r})$ is the local value of the differential tunneling conductance that is proportional to the LDOS, $g_0(E)$ is the average value of the conductance at each energy E , and θ is the angle characterizing the direction of the separation vector \mathbf{r} . Displaying $C(E, r)$ in Fig. 4A, we find a marked increase of the long-distance correlations near E_F . At this energy, the correlations remain measurable to length scales well beyond that of

single Mn acceptor states, which dominate the behavior on short length scales at all energies. The increased correlation length can also be seen directly in the size of the patches of high and low conductance (Fig. 3C). We have observed the enhanced spatial correlations near E_F for all doping levels examined in this study (up to 5%, Fig. 4B); however, this effect is most pronounced for the least doped samples (1.5%) closest to the metal-insulator transition. Control experiments on Zn-

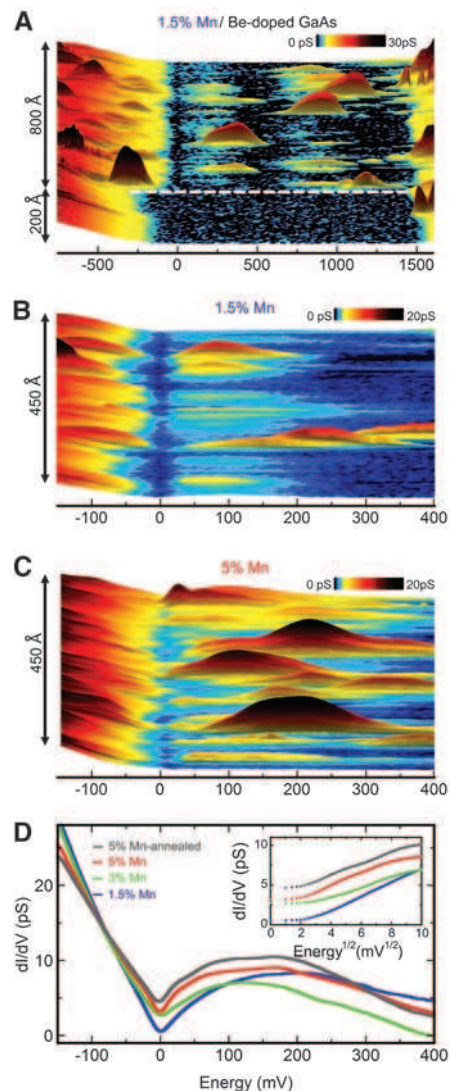


Fig. 2. Local dI/dV spectroscopy for various dopings. (A) The differential conductance (dI/dV) ($\Delta V = 10$ mV) across a line normal to the growth surface of length 1000 Å. The first 200 Å is the Be-doped GaAs buffer layer, and 800 Å of 1.5% Mn-doped GaAs follows. The junction between the two is marked by a dashed line. (B and C) The dI/dV spectra ($\Delta V = 5$ mV) for energies close to the Fermi level, across a line of length 450 Å over the 1.5% sample (B) and the 5% sample (C). Top of the valence band and the in-gap states are shown. (D) The spatially averaged differential conductance for several samples. The inset shows the same data as the main panel, with the square root of the voltage on the horizontal axis.

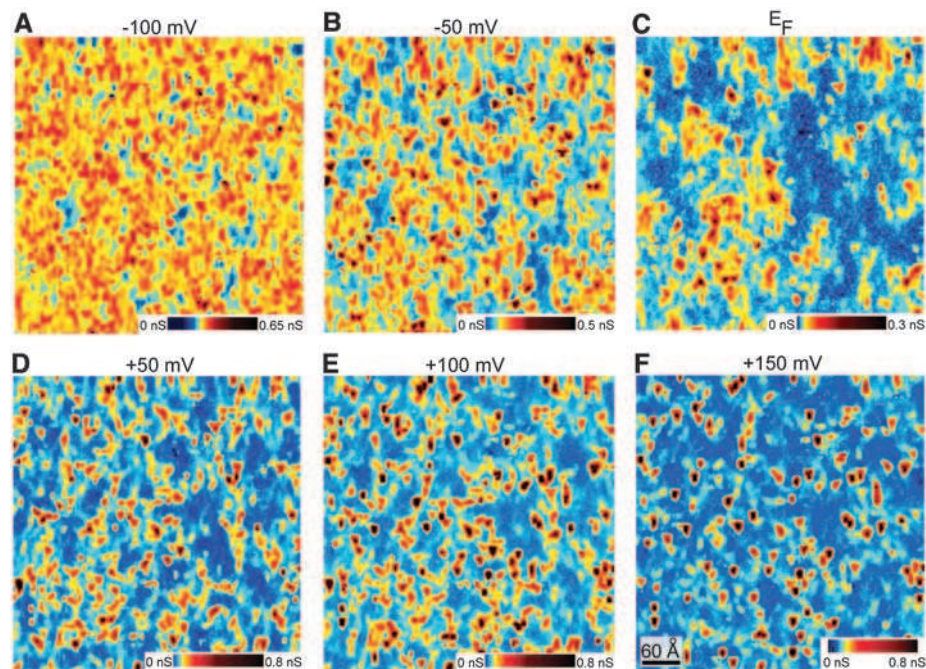
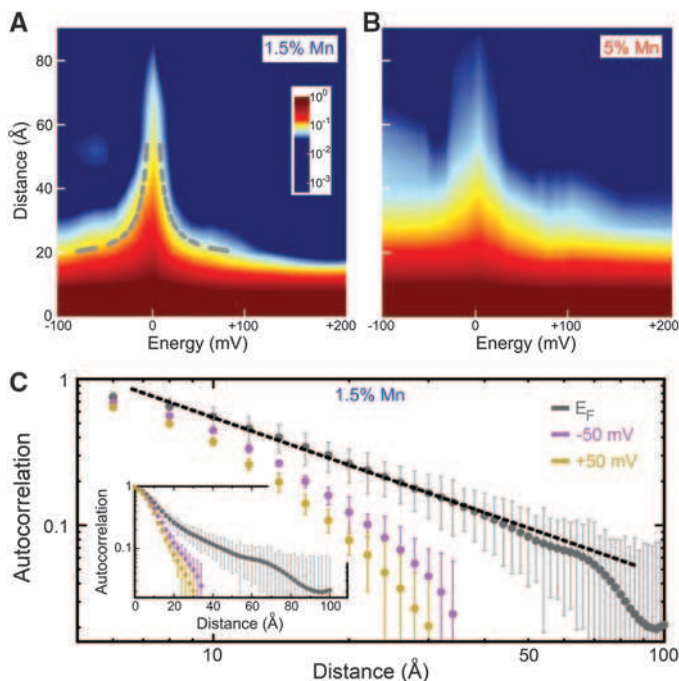


Fig. 3. Spectroscopic mapping in $\text{Ga}_{0.985}\text{Mn}_{0.015}\text{As}$. The differential conductance (dI/dV) measurements over an area of 500 Å by 500 Å show the spatial variations in the LDOS for the states in the valence band as well as states deep inside the semiconductor gap: (A) -100 mV, (B) -50 mV, (C) 0 mV, (D) +50 mV, (E) +100 mV, and (F) +150 mV.

Fig. 4. Correlation length for Mn dopings close to the metal-insulator transition. The autocorrelation was calculated from LDOS maps and is presented on a logarithmic scale for (A) $\text{Ga}_{0.985}\text{Mn}_{0.015}\text{As}$ and (B) as-grown $\text{Ga}_{0.95}\text{Mn}_{0.05}\text{As}$. The dashed line in (A) is $\sim (E - E_F)^{-1}$ and is a guide to the eye. (C) The autocorrelation for the dI/dV map at the Fermi level of $\text{Ga}_{0.985}\text{Mn}_{0.015}\text{As}$, as well as one valence band (-50 mV) and one in-gap energy (+50 mV), are plotted. The inset shows the autocorrelation for the same energies on a semi-logarithmic scale.



or Be-doped GaAs samples show no evidence of any special length scale or of a sharp peak near the E_F in the autocorrelation function.

Continuous phase transitions, such as the metal-insulator transition, are typically characterized by a correlation length, which describes the exponential decay of spatial fluctuations when a system is tuned near the phase transition. At the critical point, this correlation length diverges and spatial fluctuations and other physical properties display power-law spatial characteristics. In the noninteracting limit, the transition between a metal and an insulator occurs by tuning the chemical potential relative to the mobility edge. Mapping the spatial structure of the electronic states as a function of energy can be used to determine the correlation length and to probe the critical properties for such a transition between extended and localized states (4, 5, 8). In our experiments, the distance dependence of the energy-resolved autocorrelation function $C(E,r)$ for the 1.5% sample (Fig. 4C) appears to follow a power-law at E_F , while at nearby energies it falls off exponentially (see inset). These observations, together with the apparent divergence of the correlation at a specific energy, are indeed signatures of the critical phenomena associated with a metal-insulator transition. However, our observation that the longest-ranged correlations are centered at E_F , as opposed to some other energy, which could be identified as a mobility edge, signifies the importance of electron-electron interactions in the observed correlations.

Given the importance of electron-electron interactions, the conductance maps are perhaps more precisely identified as probing the spatial nature of quasiparticle excitations of a many-body system rather than simply imaging single-electron states in the noninteracting limit. Currently there are no theoretical models of the real-space structure of these excitations near the metal-insulator transition in a strongly interacting and disordered system, although there is continued effort to understand the nature of such transitions in the presence of interactions (5, 27). Nevertheless, we suspect that the correlation length associated with these excitations will become shorter due to multiparticle processes and inelastic effects at energies away from E_F . Our experimental results for the least conducting sample (1.5%) indicate that the correlation length ξ is indeed suppressed away from E_F , roughly following $(E - E_F)^{-1}$ (dashed line in Fig. 4A). At E_F , for this sample, these correlations decay in space following a power-law $r^{-\eta}$, with $\eta = 1.2 \pm 0.3$.

Despite the importance of strong interactions, many of the predictions for the noninteracting limit still appear to apply. Weakly disordered extended states are expected to show Gaussian distributions of the LDOS, indicating that these states have a finite probability to be present over the entire system. In contrast, near the metal-insulator transition wide distributions are expected, especially in local quantities such as the LDOS, which begin to cross over from Gaussian

to log-normal distributions even in the limit of weak localization (28, 29). Spectroscopic maps of the density of states at E_F for three different dopings (Fig. 5, A to C) show different degrees of spatial variations; however, their histograms (Fig. 5D) are similar in being skewed log-normal distributions where the mean is not representative of the distribution due to rare large values.

Decreasing the doping skews the distribution further in a systematic fashion away from Gaussian and toward a log-normal distribution. For comparison, a histogram of the LDOS for states deep in the valence band for the least doped sample (gray circles in Fig. 5D) shows a Gaussian distribution.

Based on the predictions for the noninteracting limit, we expect critical states to have a spa-

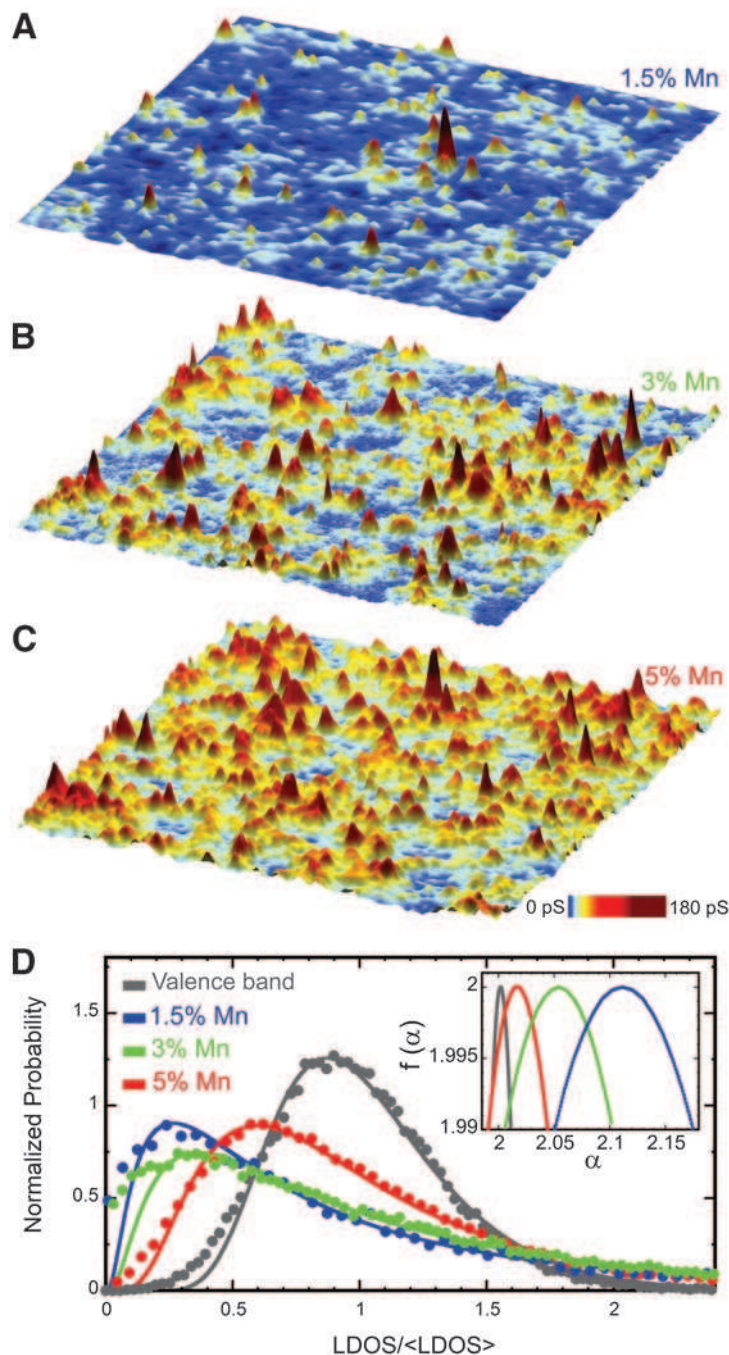


Fig. 5. The spatial variations of the LDOS at the Fermi level, with their histogram and multifractal spectrum. The LDOS mapping of a 700 Å by 700 Å area of (A) $\text{Ga}_{0.985}\text{Mn}_{0.015}\text{As}$, (B) $\text{Ga}_{0.97}\text{Mn}_{0.03}\text{As}$, and (C) $\text{Ga}_{0.95}\text{Mn}_{0.05}\text{As}$. (D) The normalized histogram of the maps presented in (A) to (C). The local values of the dI/dV are normalized by the average value of each map. The inset shows the multifractal spectrum, $f(\alpha)$, near the value α_0 where the maximum value occurs. For comparison, the results of a similar analysis over a LDOS map at -100 mV (valence band states) for the 1.5% doped sample are also shown.

tial structure that is multifractal in nature. This property is directly related to the scale-invariant nature of critical wave functions and has been examined in great detail by numerical simulations of the single-particle quantum states near an Anderson transition (8). Multifractal patterns, which are ubiquitous in nature, are usually described by analysis of their self-similarity at different length scales through their singularity spectrum $f(\alpha)$. Physically, $f(\alpha)$ describes all the fractal dimensions embedded in a spatial pattern, such as those associated with a quantum wave function and its probability distribution. It is calculated by splitting the probability distribution into sets of locations $\{r_i\}$ that share a common exponent α , where the distribution scales locally with distance as $|\Psi(r_i)|^2 \sim L^{-\alpha}$, and measuring the fractal dimension of each set (8, 21). A variety of techniques have been developed to compute $f(\alpha)$, which has been used to distinguish between various models of the Anderson transition (21, 30). Application of such an analysis to our conductance maps (Fig. 5D, inset) shows an $f(\alpha)$ spectrum that is peaked at a value away from 2, which is indicative of anomalous scaling in a two-dimensional map. The $f(\alpha)$ spectrum also shows a systematic shift with decreasing doping, indicating a trend from weak toward strong multifractality with decreasing doping. In contrast, these signatures of multifractal behavior are absent for states deep in the valence band (gray curve) that, despite the

strong disorder, show scaling consistent with those expected for extended states.

Our findings suggest that proximity to the metal-insulator transition and electronic correlations may play a more important role in the underlying mechanism of magnetism of $\text{Ga}_{1-x}\text{Mn}_x\text{As}$ than previously anticipated. Beyond its application to understand the nature of states $\text{Ga}_{1-x}\text{Mn}_x\text{As}$, our experimental approach provides a direct method to examine critical correlations for other material systems near a quantum phase transition. In principle, experiments at the lowest temperatures for samples closest to the metal-insulator transition should provide accurate measurements of power-law characteristics that can be directly compared to theoretically predicted critical exponents.

References and Notes

1. P. W. Anderson, *Phys. Rev.* **109**, 1492 (1958).
2. A. Lagendijk, B. van Tiggelen, D. S. Wiersma, *Phys. Today* **62**, 24 (2009).
3. A. Aspect, M. Inguscio, *Phys. Today* **62**, 30 (2009).
4. P. A. Lee, T. V. Ramakrishnan, *Rev. Mod. Phys.* **57**, 287 (1985).
5. D. Belitz, T. R. Kirkpatrick, *Rev. Mod. Phys.* **66**, 261 (1994).
6. S. Ilani *et al.*, *Nature* **427**, 328 (2004).
7. K. Hashimoto *et al.*, *Phys. Rev. Lett.* **101**, 256802 (2008).
8. F. Evers, A. D. Mirlin, *Rev. Mod. Phys.* **80**, 1355 (2008).
9. H. Ohno *et al.*, *Nature* **408**, 944 (2000).
10. D. Chiba *et al.*, *Nature* **455**, 515 (2008).
11. T. Dietl, H. Ohno, F. Matsukura, J. Cibert, D. Ferrand, *Science* **287**, 1019 (2000).
12. K. S. Burch *et al.*, *Phys. Rev. Lett.* **97**, 087208 (2006).
13. T. Jungwirth *et al.*, *Phys. Rev. B* **76**, 125206 (2007).

14. T. Dietl, *J. Phys. Soc. Jpn.* **77**, 031005 (2008).
15. C. P. Moca *et al.*, *Phys. Rev. Lett.* **102**, 137203 (2009).
16. S. H. Chun, S. J. Potashnik, K. C. Ku, P. Schiffer, N. Samarth, *Phys. Rev. B* **66**, 100408(R) (2002).
17. D. Neumaier *et al.*, *Phys. Rev. Lett.* **99**, 116803 (2007).
18. L. P. Rokhinson *et al.*, *Phys. Rev. B* **76**, 161201 (2007).
19. B. L. Sheu *et al.*, *Phys. Rev. Lett.* **99**, 227205 (2007).
20. R. C. Myers *et al.*, *Phys. Rev. B* **74**, 155203 (2006).
21. Materials and methods are available as supporting material on Science Online.
22. D. Kitchen, A. Richardella, J. M. Tang, M. E. Flatté, A. Yazdani, *Nature* **442**, 436 (2006).
23. J. K. Garleff *et al.*, *Phys. Rev. B* **78**, 075313 (2008).
24. J. M. Tang, M. E. Flatté, *Phys. Rev. Lett.* **92**, 047201 (2004).
25. T. O. Strandberg, C. M. Canali, A. H. MacDonald, *Phys. Rev. B* **80**, 024425 (2009).
26. B. L. Altshuler, A. G. Aronov, *Solid State Commun.* **30**, 115 (1979).
27. D. M. Basko, I. L. Aleiner, B. L. Altshuler, *Ann. Phys.* **321**, 1126 (2006).
28. I. V. Lerner, *Phys. Lett. A* **133**, 253 (1988).
29. B. L. Altshuler, V. E. Kravtsov, I. V. Lerner, *Phys. Lett. A* **134**, 488 (1989).
30. A. Chhabra, R. V. Jensen, *Phys. Rev. Lett.* **62**, 1327 (1989).
31. This work was supported by grants from Office of Naval Research, Army Research Office, the Keck Foundation, NSF, and the NSF–Materials Research Science and Engineering Center program through the Princeton Center for Complex material. P.R. acknowledges a NSF graduate fellowship.

Supporting Online Material

www.sciencemag.org/cgi/content/full/327/5966/665/DC1

Materials and Methods

Figs. S1 to S4

References

21 October 2009; accepted 5 January 2010

10.1126/science.1183640

A Coherent Beam Splitter for Electronic Spin States

J. R. Petta,^{1*} H. Lu,² A. C. Gossard²

Rapid coherent control of electron spin states is required for implementation of a spin-based quantum processor. We demonstrated coherent control of electronic spin states in a double quantum dot by sweeping an initially prepared spin-singlet state through a singlet-triplet anticrossing in the energy-level spectrum. The anticrossing serves as a beam splitter for the incoming spin-singlet state. When performed within the spin-dephasing time, consecutive crossings through the beam splitter result in coherent quantum oscillations between the singlet state and a triplet state. The all-electrical method for quantum control relies on electron–nuclear spin coupling and drives single-electron spin rotations on nanosecond time scales.

Energy-level crossings, in which two quantum states cross in energy as a function of an external parameter, are ubiquitous in quantum mechanics (1). Coupling of the quantum states provided by tunnel coupling with strength Δ , for example, leads to hybridization of the states and results in an anticrossing with a minimum energy splitting 2Δ (2, 3). Passing a quantum state through an anticrossing in the level diagram will result in a sweep-rate-dependent nonadiabatic

transition probability P_{LZ} , commonly known as the Landau-Zener probability (4). The theory of Landau-Zener transitions can be applied to a diverse set of problems, ranging from electronic transitions in molecular collisions to chemical reactions to neutrino conversion in the sun (5). We apply Landau-Zener transition physics to coherently control electronic spin states in a semiconductor double quantum dot (DQD).

Semiconductor quantum dots have emerged as promising platforms for quantum control of charge and spin degrees of freedom (6). Considering future applications of electron spin qubits in quantum information processing, the required elementary building blocks are the exchange gate, which couples two spins, and single-spin rotations

(7). Extremely fast 200-ps exchange gates have been demonstrated (6, 8). However, coupling to the small magnetic moment of the electron (as required for single-spin rotations) is much more difficult, leading to relatively long, ~ 100 -ns gate-operation times in GaAs quantum dots (9). In addition, the ac magnetic fields required for single-spin electron spin resonance (ESR) are difficult to localize on a single quantum dot (~ 40 nm), hindering extension of the method to a large number of quantum dots operating in close proximity. Several groups have demonstrated fast optical control of single spins, but these methods are also difficult to apply locally (10, 11). In principle, local rotations can be achieved with the use of electrically driven spin resonance, which requires spin-orbit coupling and an ac electric field, but the Rabi frequencies obtained in GaAs quantum dots are approximately a factor of 2 slower than those obtained using conventional ESR (12, 13). We demonstrate an all-electrical method for driving local single-spin rotations on nanosecond time scales.

Our method for coherent quantum control of electron spins is based on two consecutive sweeps through a singlet-triplet anticrossing in a DQD energy-level diagram. Coherent oscillations between the singlet and $m_s = +1$ triplet state, T_+ , occur on a nanosecond time scale and are made possible by the hyperfine interaction between the trapped electron spins and the nuclear-spin bath (14–16). The oscillations are controlled by tuning the external magnetic field B_E and the voltage

¹Department of Physics, Princeton University, Princeton, NJ 08544, USA. ²Materials Department, University of California at Santa Barbara (UCSB), Santa Barbara, CA 93106, USA.

*To whom correspondence should be addressed. E-mail: petta@princeton.edu